ChemElectroChem

Research Article
doi.org/10.1002/celc.202400062

Chemistry Europe
European Chemical Societies Publishing

www.chemelectrochem.org

In Situ Determination of the Potential Distribution within a Copper Foam Electrode in a Zinc-Air/Silver Hybrid Flow Battery

Sascha Genthe,*[a, b] Luis F. Arenas,[a, b] Maik Becker,[a, b] Ulrich Kunz,[a, b] and Thomas Turek[a, b]

This work describes a novel methodology for measuring the potential distribution within the porous copper foam electrode of a zinc-air/silver hybrid (ZASH) flow battery by using local potential probes. The suitability of dynamic hydrogen electrodes (DHEs) and a quasi-reference electrode as probes is evaluated, with the latter chosen in view of stability. Liquid and solid-phase potentials are recorded at varying applied current densities over multiple charge-discharge cycles. Various zinc structures are found within specific overpotential ranges, with moss-like structures appearing between 7.8 mV and 13.2 mV and the desired boulder structures in the range of 22 mV to 100 mV. Regardless of the current density, the highest liquid-phase potentials are always measured in the outermost region of the porous foam near to the separator. In practice, this means that increasing the thickness of the copper foam over about 5 mm does not provide significant performance benefits. Conversely, solid-phase potentials across the copper foam remain nearly uniform, resulting in negligible effects on local overpotential. The presented technique provides unique insights into the behavior of porous electrodes in electrochemical energy conversion technologies, facilitating the determination of the optimal properties for maximum efficiency, such as electrode thickness.

Introduction

Deployment of sustainable energy storage technologies has become an urgent global challenge given the need to mitigate climate change, decrease greenhouse gas emissions, and provide a reliable energy supply for a fast-growing population while harnessing intermittent renewable power sources.[1] Future achievement of all of these targets requires multidisciplinary efforts. In this regard, electrochemical energy storage represents a critical factor in the evolution to a cleaner and more sustainable energy infrastructure.[1,2]

On the path towards this transformation, zinc-based batteries could prove to be a key element in meeting the growing demand for efficient, environmentally friendly energy storage.[3–5] In particular, zinc-based flow batteries have several advantages in scalability and service mode flexibility over conventional static batteries.[3,6] However, their full potential in terms of scalability and wide application is limited by persistent problems, particularly dendrite formation during charging, passivation during discharging, and undesirable shape changes at the negative zinc negative electrode.[7–10]

To overcome these challenges, several studies on the improvement of zinc-based batteries[11–17] recommend the use of highly porous 3D electrodes as substrate for the negative zinc electrode. In particular, commercially available metal foams with their open-cell structures are promising candidates when it comes to avoiding restrictions on mass transfer due to short diffusion paths to the electrode surface and thus also helping to prevent dendrite growth.[11,15] In addition, the high electronic conductivity of the network of interconnected pores can prolong the cycle stability of the battery by avoiding shape change effects at the zinc electrode.[9,18,19] The application of metal foam as negative electrode substrate has been successfully demonstrated in some zinc-based flow batteries.[16,17]

An important challenge to the development of zinc-based flow batteries with negative metal foam electrodes is the analysis and control of the potential distribution in the interior of the porous material, which is critical to achieve homogeneous and dendrite-free zinc deposits, avoid cell voltage losses due to high overpotentials and ohmic losses as well as to prevent parasitic reactions.[3,6]

[a] S. Genthe, Dr. L. F. Arenas, Dr. M. Becker, Prof. Dr. U. Kunz, Prof. Dr. T. Turek
Institute of Chemical and Electrochemical Process Engineering
Clausthal University of Technology
Leibnizstraße 17, 38678 Clausthal-Zellerfeld, Germany
and
Present Address: S. Genthe is now at
Robert Bosch GmbH Zentrum für Forschung und Vorausentwicklung
Robert-Bosch-Campus 1, 71272 Renningen, Germany
E-mail: genthe@icvt.tu-clausthal.de

[b] S. Genthe, Dr. L. F. Arenas, Dr. M. Becker, Prof. Dr. U. Kunz, Prof. Dr. T. Turek
Research Center Energy Storage Technologies
Clausthal University of Technology
Am Stollen 19A, 38640 Goslar, Germany
and
Present Address: Dr. L. F. Arenas is now at
Research Group Applied Electrochemistry & Catalysis
University of Antwerp
Universiteitsplein 1, 2610 Wilrijk, Belgium

Supporting information for this article is available on the WWW under https://doi.org/10.1002/celc.202400062

In fact, the study of potential distribution at porous electrodes has been a major task of electrochemical engineering for decades.[20] Regarding zinc-based batteries, Coleman recognized as early as the 1950s that the current distribution and thus the metal deposition within them is not uniform.[21] This approach involved a cell with a porous electrode divided into compartments. By introducing a carbon rod into each of them, conversion currents were measured, revealing that the current inside the electrode was notably lower than in its outer regions.

Studies on the utilization of porous electrodes continued since and moved towards the consideration of metal foams.[22–26] In addition to direct measurement of current distribution, other techniques were used in these studies to determine the activity within the electrode. For instance, in one approach the potential distribution along the electrode was measured with reference electrodes through glass probes,[22,26] while in another approach the electrode was cut into thin slices after the experiment to analyze the reaction products.[22,24] Regardless of the technique, however, all of the studies confirm the relevance of potential distribution at porous electrodes and provide insights into the impact of various parameters on it such as electrode thickness. The general conclusion from such studies remains equally valid today: the optimal utilization of a porous electrode requires small thickness and low current density in combination with high conductivities of the electrolyte and the electrode matrix.[22]

Progress has followed by using analytical models to describe potential distribution at the electrodes in question under flowing electrolytes.[27–29] Meanwhile, the latest developments have used 3D models and finite element solvers to combine electrode kinetics and electrolyte hydrodynamics at planar,[30,31] and 3D or porous substrates. Metal deposits can then be evaluated through advanced imaging techniques.[32,33] Yet, experimental measurements at foam electrodes remain critical to validate these models for modern energy storage technologies.[34] These validations are challenging, mainly due to the fact that local liquid-phase potentials at different points along and across the metal foam are considerably difficult to measure in practice. Moreover, local current and potential distributions reside, fundamentally, within the irregular polyhedral cells (each of their sides is an open pore) that form such cellular foam materials.[33,35]

Thus, the application of potential probes in the liquid-phase within individual cells or pores in the porous material is the most suitable measurement technique since no destructive analysis of the electrodes is necessary and the challenging operation of complex ad hoc electrochemical cell designs is eliminated. For instance, the use of flexible dynamic hydrogen electrodes (DHEs) in zinc-based systems has become increasingly popular due to their good handling in a wide and dynamic pH range.[36–42] A DHE consists of two electrodes electrically connected to a power supply and a high ohmic resistance.[43,44] Submerging this potential probe in an electrolyte results in the formation of a thin hydrogen layer on the cathode, ensuring a stable potential and thus serving as a reliable reference. DHEs were already successfully tested in several battery applications and enabled a highly accurate measurement of the potentials in the electrolyte, especially in vanadium flow batteries[39,40,45,46] and fuel cells[47–50] as well as water electrolysis applications.[41]

Another candidate for implementation as potential probe in a porous material is the quasi-reference electrode, which consists solely of a platinum wire.[51] In contrast to the design of a DHE, the quasi-reference employs a single metal wire and simplifies the experimental arrangement. Nevertheless, quasi-reference electrodes have been widely adopted in several flow batteries[52–55] and fuel cells[56,57] and are considered as a suitable reference electrode in adequate conditions. An advantage of using either a DHE or a quasi-reference instead of a Hg/HgO reference fitted to a relatively thick glass or plastic capillary is that the gas evolving nature or the wire probe make them very resistant to irregular blockage by bubbles or particles present in the flowing electrolyte. Plus, the wire probes can have a small diameter compatible with the dimensions of the individual cells that form many foam materials.

In this study, we demonstrate the close relationship between the potential distribution in a porous metal foam and the zinc structures formed therein during the operation of a zinc-air/silver hybrid (ZASH) flow battery. To achieve this aim, potential probes were placed in situ within individual cells at different points of the porous metal foam that constitutes the negative electrode of the ZASH flow battery. To the best of our knowledge, this is the first time that the liquid-phase potential measurement has been performed locally in metal foam electrodes. Experiments were carried out in a cell design optimized since our previous study[17] to allow a simple positioning of the potential probes inside a metal foam with a thickness of 20 mm. The results presented here include experiments on the applicability of DHEs and a quasi-reference electrode as liquid-potential probes in a zinc-containing electrolyte. We also reveal the influence of oxidation processes at the positive gas diffusion electrode (GDE), which occur during charging, on the overpotentials at the negative metal foam electrode. In summary, we present a novel determination of potential distribution in situ within a porous metal foam electrode over several charge-discharge cycles in a zinc-based flow battery. The results provide insights into the utilization of porous electrodes and enable conclusions about the optimal electrode thickness for practical applications.

Results and Discussion

Stability of Different Potential Probes

The designs of the flow cell (Figure 1a) and the in-house developed potential probe (Figure 1b) were inspired by the design considerations of DHEs from several studies.[38,39,48,49] Modifications for the use in a highly alkaline electrolyte in combination with a porous metal foam were necessary, which are described in the following. The potential probes consist of a positive electrode (PE), a negative electrode (NE) and an ohmic resistance that limits the electrical current. These electrodes were connected to a standard 9 V primary battery. When both

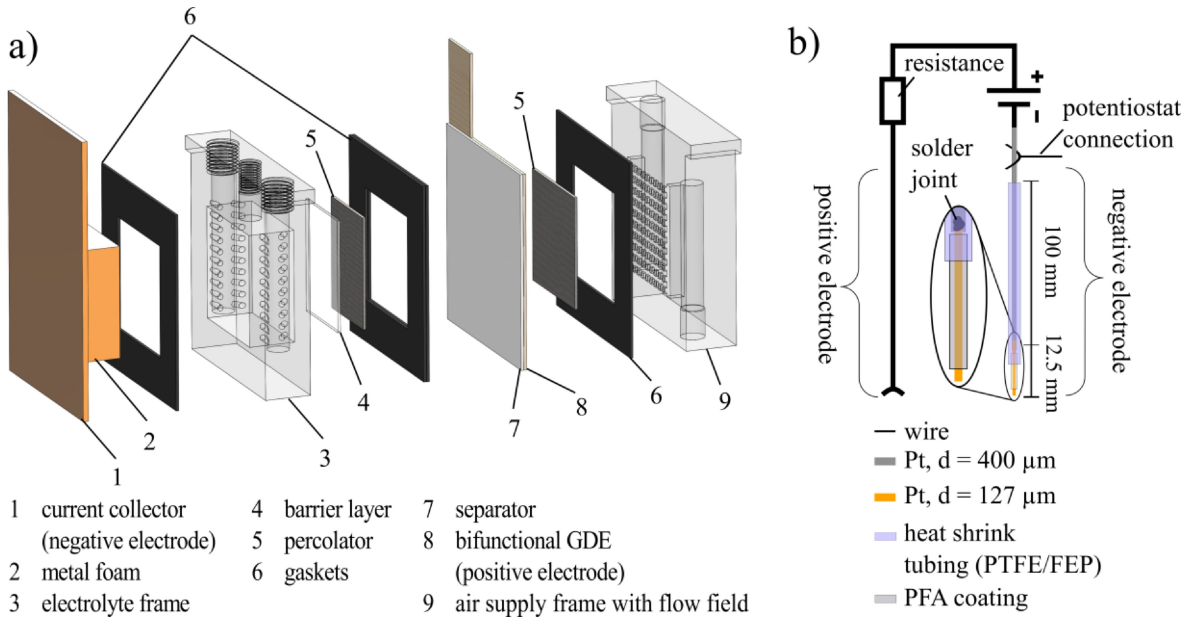

Figure 1. A modified ZASH flow battery and dynamic probe for the measurement of liquid-phase potential. a) Exploded view of the electrochemical flow cell and b) schematic view of a DHE.

electrodes come into contact via an alkaline electrolyte, water electrolysis begins. The intensity of the reaction at the electrodes is limited by the resistance, as described below. The evolving hydrogen in the vicinity of the NE leads to a reducing regime that protects the electrode from oxidation. Therefore, the NE of the DHE is preferred to be used as a reference electrode.[39,46,48] For the fabrication of the PE of the DHE, a flexible sensing lead with a connector (MSB-200, Voltcraft, Germany) was soldered to one end of the resistance. An alligator clip was used to connect the lead to any electrically conductive material that is part of the battery under investigation, and that is in contact with the electrolyte, e.g., the current collector of the cell (Figure 1a), which then becomes the PE of the probe.

A schematic diagram of the design of the quasi-reference electrode is not shown, as this probe solely consists of the equivalent of the NE of a DHE without modifications. This means that no additional battery, no ohmic resistance and therefore no PE is required to use this potential probe. In contrast to the NE of the DHE, no hydrogen is formed at the probe tip of the quasi-reference electrode in alkaline media as there is no power supply. Instead, Bagotzky et al.[58] found that platinum undergoes a corrosion process forming the soluble complex $[Pt(OH)_6]^{2-}$ in a 1 M KOH at 20 °C. In a long-term test over hundreds of hours, they set the electrode potential to 1.05 V vs. RHE and measured a corrosion rate of 10^{-4} A m^{-2} at the beginning, which decreased quickly in the first 4 hours to 10^{-6} A m^{-2} and then stabilized. The corrosion of platinum in alkaline media was also observed by other research groups at similar conditions.[59–61] However, due to the rapid stabilization behaviour and the negligible corrosion rate described above, we decided to use platinum as the probe material.

The fabrication of the NE for both types of probe required more effort in the choice of materials due to the direct contact with the KOH-containing electrolyte and its high tendency to creep through even the smallest gaps and channels.[62] For this purpose, chemical-resistant dual heat shrink tubing (PTFE/FEP, Reichelt Chemietechnik, Germany) was used as insulation for the electrode connection wire (Figure 1b). The shrink tube consists of two concentrical tubes whose outer material is polytetrafluoroethylene (PTFE) and whose inner tube is made of fluoroethylenpropylene (FEP). It reduces its inner diameter during heating and thus completely encloses the material inside. A platinum wire with a diameter of 400 µm (R. Götze, Germany) was used as an electrode connection. At the end of this wire, which is also entirely enclosed by the shrink tube, an additional polymer-coated thinner platinum wire with a diameter of 200 µm (with coating) (PT-5T, Science Products GmbH, Germany) is soldered as the active electrode of the probe. Its coating is also chemical-resistant as it is made of perfluoroalkoxy alkane (PFA). About 1 mm of the coating at the tip of the probing wire was removed with the help of a gas burner. The diameter of the tip thus exposed is about 127 µm. The liquid-phase potential at this point is given by the measured potential difference between the probe tip and the metal foam. Additionally, two solid-phase potential probes were placed at the ends of the foam electrode. Their design is less complex compared to that of the liquid-phase potential probes since they do not involve HER nor platinum corrosion. These probes consist of a single platinum wire ($d = 400$ µm), with their tip directly soldered to the metal foam and insulated with the heat shrink tubing described above.

Figure 2a shows the arrangement of the liquid (L) and solid (S) phase potential probes at the porous metal foam. Figure 2b provides a photo of the electrode after the probes were

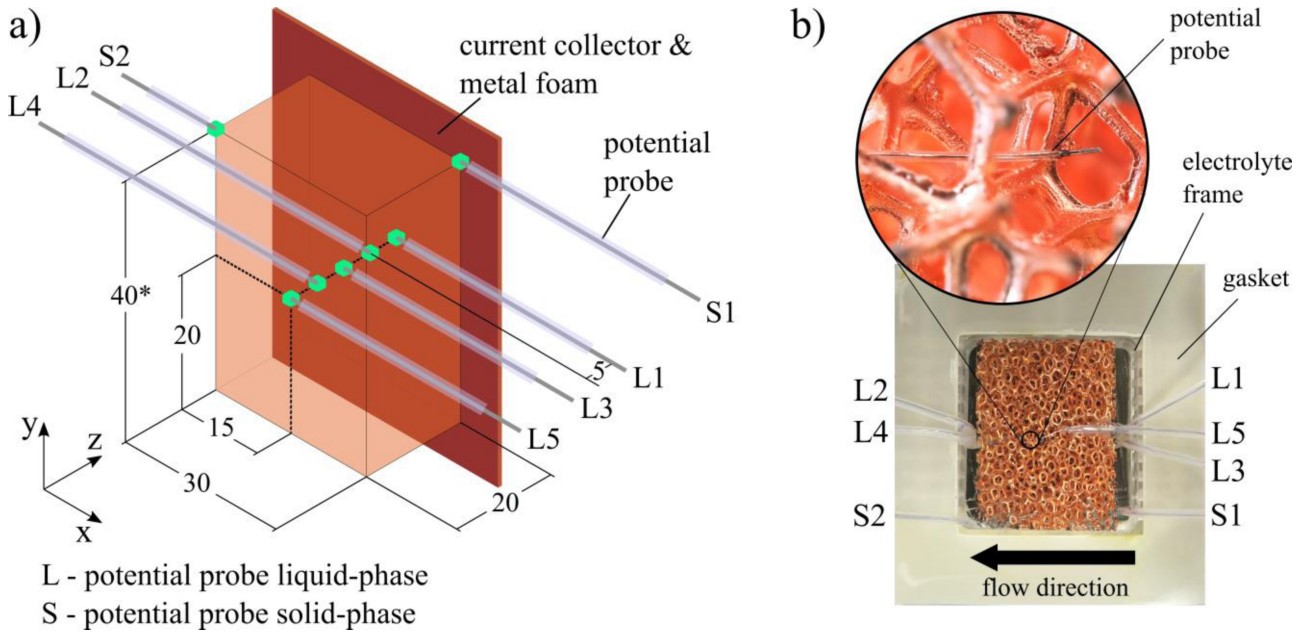

Figure 2. Integration of potential probes into the porous metal foam negative electrode. a) Schematic view of the arrangement of the liquid-phase (L1–L5) and solid-phase potential probes (S1–S2). Green markings indicate the probe tip and, thus, the location of the potential measurement (lengths are given in mm). b) Metal foam with potential probes inserted into the electrolyte frame of the full cell. The magnified section shows the active tip of the NE of the liquid-phase potential probe placed within an individual foam pore.

inserted. Five liquid-phase potential probes (L1–L5) were introduced into the metal foam on the same *xz*-plane. The tips of the probes were located in the middle of a foam pore without contact with the solid-phase (Figure 2b). The distance between the probes was 5 mm. Therefore, the outermost probe L5 was positioned at a distance of 20 mm from the current collector and probe L1 is directly located at the current collector at 0 mm. The parts of the probes insulated by the heat shrink tubing were glued to the surface of the metal foam with a two-component epoxy adhesive (UHU, Germany) to prevent a position shift during cell assembly and operation. In some experiments, two solid-phase potential probes (S1–S2) were placed at the bottom and the top of the metal foam to examine the overpotentials at the copper foam during charging.

Figure 3 shows a scheme of the experimental arrangement for the stability tests of the liquid-phase potential probes. The test vessel was a beaker filled with 400 mL of an electrolyte consisting of 30 wt% KOH, and 2 wt% dissolved ZnO. The beaker was hermetically sealed with Parafilm M (Amcor, Australia) from the environment and constantly purged with nitrogen to prevent the ingress of carbon dioxide. A PTFE-coated stirring magnet was used to simulate the convective flow in the battery in Figure 1a.

The stability tests aimed to identify the optimum resistance required for the DHE circuit in a range from 10 MΩ to 14.7 MΩ to ensure a constant potential at the positive electrode of the probes over several hours. Meeting this important criterion guarantees the use of a reliable reference electrode. For a block battery of 9 V and standard carbon composition resistors (Conrad, Germany) of 10 MΩ, 13 MΩ and 14.7 MΩ, the currents

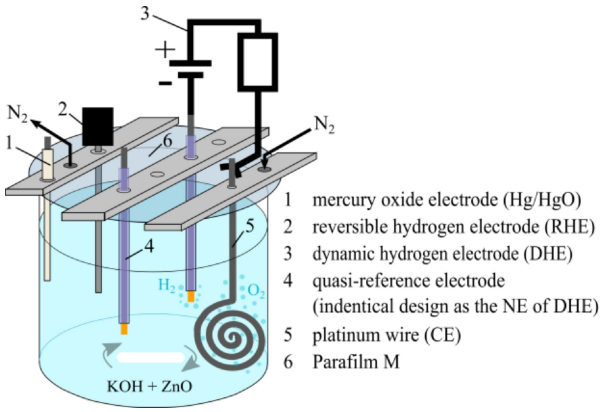

Figure 3. Electrochemical cell for the evaluation of different potential probes. The RHE was used as reference electrode for the in-house developed potential probes. A Hg/HgO reference was used to verify that the RHE provides reliable results.

in the electric circuit are 0.9 μA, 0.69 μA and 0.61 μA, respectively.

To enable the desired hydrogen evolution reaction at the NEs, the PEs of the DHEs were connected to a platinum wire spiral, which is used as the counter electrode (CE) (Figure 3). The potentials of the NEs were measured against a commercially available reversible hydrogen electrode (RHE) (Mini-HydroFlex, Gaskatel, Germany). A mercury oxide reference electrode (Hg/HgO) (RE-61AP, ALS Co., Japan) was used to detect possible potential fluctuations of the RHE. Critically, we also evaluated a quasi-reference electrode only consisting of the equivalent to the NE of the DHE as liquid-phase potential probe (Figure 1b) in

order to examine the potential without the need or influence of the electrical current used in the relatively complex DHE.

Figure 4 shows the potential curves of the NEs of four different (three DHEs, one quasi-reference) liquid-phase potential probes with different resistances and a commercially available Hg/HgO reference electrode, measured against the RHE over 15 h. The potential curve of Hg/HgO vs. RHE confirms that the potential of the RHE did not change from its initial value of about 0.977 V during the experiment. This proves that any influence of the RHE on occurring potential changes can be neglected. Furthermore, it can be recognized that the potential of the DHE liquid-phase potential probes increases with higher resistances. This happens because higher resistances lower the current in the electric circuit of the probe and decrease the hydrogen evolution rate at the positive electrode. Besides that, the value of the resistance has a major influence on the potential stabilization of the probe over time, which is crucial for the application as a reference.

As seen in Figure 4 the DHE probe with the lowest resistance of 10 MΩ showed the lowest initial potential at about −0.13 V and the highest potential gradient over time. In the literature, the time period in which a potential gradient occurs is referred to as an initialization time and is due to the reduction of oxygen and surface oxides at the probe tip.[43,63] Using a resistance of 13 MΩ produced the expected shift of the initial potential to higher values of about −0.08 V due to a decreased current in the electric circuit. An increase of the resistance to 14.7 MΩ revealed that the potential gradient is significantly lower compared to the probes with lower resistances. In addition, the initial potential shifted to values near 0.9 V, which is about 1 V higher than the initial potential of a probe with 13 MΩ. This behavior is unexpected and most likely due to a perturbation of the hydrogen film at the tip of the PE and the adsorption of oxygen.[43,44] This can be caused when the current is too low, as set by a high resistance.

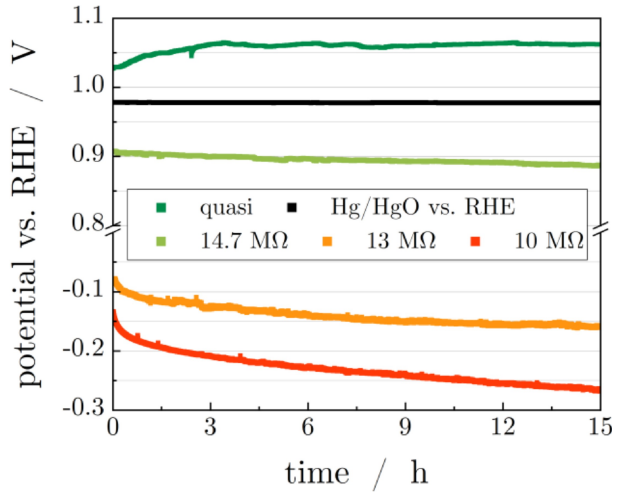

Figure 4. Stability of the measured potentials of in-house developed liquid-phase potential probes. The resistances within the electric circuit of the probes were varied to examine the influence on the potential stabilization. The quasi-reference configuration was selected for stable measurements.

Besides the potential differences at the DHE probes, we observed a slight color change of the tip of the NE of the probes from a silvery shiny surface to a gray matte surface. This was seen in particular at the probes with the resistances of 10 MΩ and 13 MΩ, which show a potential below 0 V against RHE. In a repetition experiment with a similar 10 MΩ potential probe operated for 50 hours under similar conditions, the structural change became more evident (Figure S1a, b). A likely reason is that zincates are adsorbed on the probe tip, followed by a reduction reaction to zinc. These processes may cause an error in the reference electrode, which has been observed for other electrochemical systems in the literature.[43,44,48] The comparison of DHE probe potentials in the following provides more clarity. The measured potential of the probe using a resistance of 10 MΩ is about −0.266 V against RHE at the end of the experiment, with a strong tendency to decrease further. We measured an open cell voltage of a porous zinc-plated electrode of −0.430 V against RHE at similar conditions in previous work.[17] The closeness of both values and the fact that the potential of the 10 MΩ probe had not yet stabilized after 15 hours support our hypothesis that zinc deposition may have already occurred in addition to zincate adsorption. In contrast, and as shown in Figure 4, a quasi-reference electrode afforded a much more stable potential of approximately 1.063 V after 4 h and remained almost unchanged for the rest of the experiment. Therefore, we decided to use this type of reference electrode as a liquid-phase potential probe for the full-cell experiments to prevent zinc deposition errors and the progressive shift of potential value of the DHE probes. The functionality of each of the in-house developed probes was tested before each flow cell experiment by performing a hydrogen evolution reaction at the electrode tip in an alkaline electrolyte consisting only of 30 wt% KOH. The resting potential of the probes was then measured with a voltmeter for several minutes against a RHE. When the measured potential was close to 1 V, the probe was rinsed and fixed to the center of a pore in the metal foam electrode of the battery.

Qualitative Impact of Current Density on Foam Electrode Utilization

As shown in Figure 5, the zinc deposition is inhomogeneous within the metal foams, seen as different colored areas. The foam samples were taken after an additional charging process conducted after five complete charge-discharge-cycles and current interrupt (CI) measurements at a capacity of 1.2 Ah. The preparation of the foams for examinations was made by cutting the foams along the *xz*-plane at a height (*y*-axis) of 20 mm (Figure 2a) with a blade from a cutter knife. The yellow dots indicate the positions of the tips of the liquid-phase potential probes L1–L5 (0 mm–20 mm). Exposed copper areas resulting from cutting the foam are ignored in these observations.

The inhomogeneity of zinc deposition is particularly evident at the current densities of 50 mA cm^{-2} and 90 mA cm^{-2}. In contrast, the zinc deposition seems more homogenous across the foam operated at 130 mA cm^{-2}. To assess the amount of

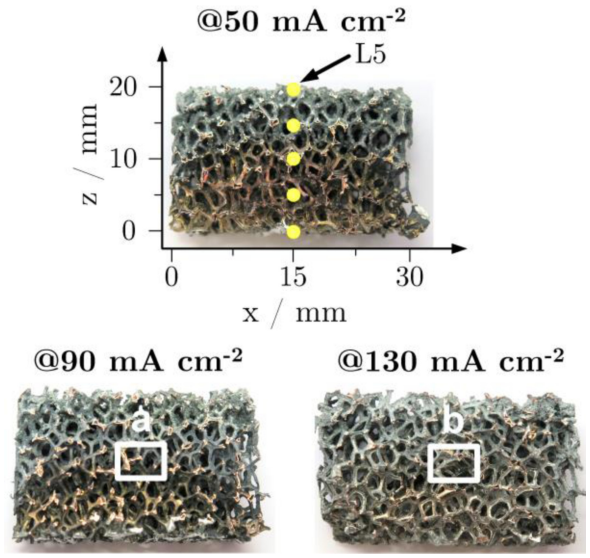

Figure 5. Cross-section of porous copper foams along the xz-plane (Figure 2a). Foam samples were taken after the charging processes, which were performed at current densities of 50 mA cm^{-2}, 90 mA cm^{-2}, and 130 mA cm^{-2}, respectively. The charged capacity was 1.2 Ah in each case. The yellow markings indicate the location of the tips of the liquid-phase potential probes L1–L5 (0 mm–20 mm), with the outermost probe L5 positioned at 20 mm. The rectangles marked with the letters (a) and (b) correspond to sections examined in more detail with the 3D microscope (Figure S2a, b).

deposited zinc more accurately, the foam samples operated at 90 mA cm^{-2} and 130 mA cm^{-2} were qualitatively examined with a microscope. Therefore, comparable locations on the foam samples were chosen indicated by (a) and (b) at a width (*z*-axis) of about 10 mm (Figure 2a). These areas correspond to the position of the tip of the probe L3. The magnified images of these regions (Figure S2a, b) confirm that at the higher current density of 130 mA cm^{-2}, zinc deposition within the metal foam is more prominent. This is shown by the intense gray metallic color. The coating thickness appears to be very thin. However, comparing the section of the foam sample operated at 90 mA cm^{-2} (Figure S2a) with a copper foam before any charge or discharge (Figure S2c), it becomes clear that zinc is also present, but it does not completely cover the surface of the foam struts as at 130 mA cm^{-2} (Figure S2b). This finding also appears to hold for operation at a current density of 50 mA cm^{-2} when comparing the color of the foam sample (Figure 5) at the widths (*z*-axis) of 0 mm to 10 mm with the initial color of a pristine foam (Figure 2b).

It becomes evident that increasing the current density has only a limited effect on zinc distribution within the porous copper foam. It follows that the flow battery capacity cannot be increased by simply choosing a thicker electrode, since the highest activity occurs near the counter electrode. The observed activity gradient across the foam thickness can be confirmed by numerous studies on the theoretical and practical investigation of metal deposition in porous electrodes.[20–22,26,64–66] The reason for this distribution of deposited zinc is the heterogeneous potential distribution across the metal foam (*z*-axis in Figure 2a), which depends on the kinetics and the ohmic resistances of the electrode and electrolyte.[64]

Influence of the Solid-Phase Potential on the Local Overpotential

As seen in Figure 6a, b the solid-phase potentials φ_S measured at the probes S1 (0 mm) and S2 (20 mm) (Figure 2a) during five charging cycles did not differ significantly at a current density of 130 mA cm^{-2}. The measured overpotentials show the shape of measurement noise points, mainly caused by the sensitive potentiostat detecting minor changes in the system at the submillivolt range. Indeed, the solid-phase potentials measured at both probes were always below 0.4 mV, which means a

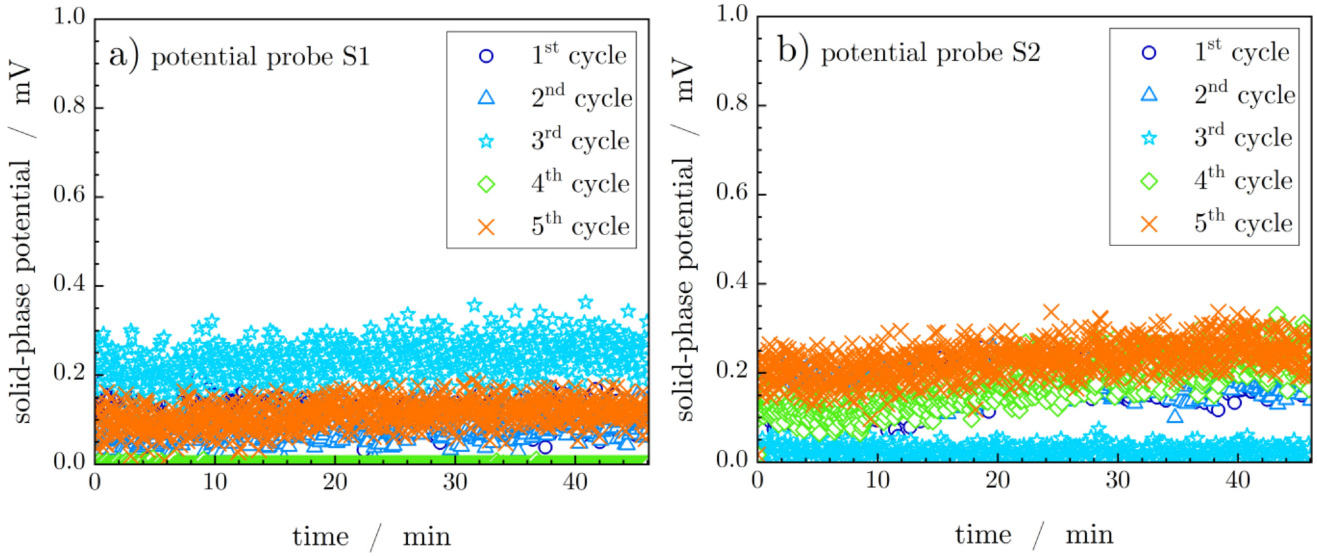

Figure 6. Solid-phase potentials measured at a current density of 130 mA cm^{-2} during five charge cycles. a) Potentials measured at probe S1, which is positioned at the bottom of the foam at 0 mm. b) Potentials measured at probe S2, which is positioned at the top of the foam at 20 mm.

negligible influence on the local overpotential, η. This finding was expected due to the high electrical conductivity of the copper metal foam. Consequently, the liquid-phase potential φ_L is determining the local overpotential according to Equation (1).

$$\eta = \varphi_S - \varphi_L - E_{eq} \quad (1)$$

Here, parameter E_{eq} is the equilibrium potential measured between the probe tip and a single pore strut in the metal foam. Since the metal foam did not exhibit high overpotentials at probes S1 (0 mm) and S2 (20 mm) at a current density of 130 mA cm^2, no further experiments were performed at the lower current densities of 50 mA cm^{-2} and 90 mA cm^{-2}. In other words, the ohmic drop across the metal foam electrode and its contribution to electrode overpotentials are negligible for these dimensions owing to the very high conductivity of copper.

Liquid-Phase Potentials and Corresponding Zinc Structures

The liquid-phase potentials measured during five charge-discharge cycles and the structure of zinc deposits after one additional charging cycle near the probe tip are examined in this section. Due to the large amount of data, the following discussion is focused on the results from the experiments at the lowest and highest current density of 50 mA cm^{-2} and 130 mA cm^{-2}, respectively (Figure 7 and Figure 8). The results of the experiment at the intermediate current density of 90 mA cm^{-2} are displayed in Figure S5.

The liquid-phase potentials recorded with the quasi-reference probes are illustrated in 3D plots in Figure 7a and Figure 8a. For clarity, the measured potentials of each probe are separately displayed in Figure S3a–e and Figure S8a–e. Reproducibility was ensured by repeating the experiments with the same setup but changing the probes, the electrolyte and cell components (metal foam, GDE, etc.) each time. The results of the repeated experiments are shown in Figure S3f–j and Figure S8f–j. The results for the experiments conducted at a current density of 90 mA cm^{-2} are also shown in Figure S7a–e and Figure S7f–j, respectively. Recorded liquid-phase potentials are discussed just below, after presenting the zinc morphology relevant to such results.

Indeed, the evaluation of the SEM images centers around the zinc deposits at the probes L3–L5 (Figure 7b and Figure 8b). This is due to the negligible utilization of the metal foam near the probes L1 and L2 below a width (*z*-axis) of 10 mm (Figure 2a), as shown in a previous section in Figure 5. For completeness, the SEM images of the zinc deposits near the probe tips of L1 and L2 are shown in Figure S9.

According to the literature, the formation of specific zinc morphologies is dependent on the applied current density and the resulting overpotentials at the zinc electrode.[67–69] The reported liquid-phase potentials for the formation of mossy, boulder and dendritic structures in an alkaline solution of KOH with dissolved ZnO are summarized in Table 1. Despite many differences in electrolyte composition and used reference electrode, the potential ranges for the different zinc structures are clearly recognizable. Moss-like structures are observed at low overpotentials in the range of 10 mV to 30 mV. Boulder structures are formed at a moderate overpotential range of 30 mV to 140 mV. Dendrites are produced under an overpotential range of 75 mV to 320 mV. The overlapping ranges for the formation of boulder structures and dendrites are presumably originated by the different experimental conditions and testing times. However, the determined ranges have a sufficient accuracy, which is shown in the following.

As seen in Figure 7a, the measured liquid-phase potentials at the probes L1–L5 (0 mm–20 mm) at a current density of

Table 1. Overpotentials for the formation of mossy, boulder and dendritic zinc structures in alkaline electrolytes containing KOH and dissolved zinc.

KOH concentration		Zinc concentration	Reference electrode	Overpotential mossy	Overpotential boulder	Overpotential dendrite	Ref.
Mol L^{-1}	wt%	Mol L^{-1}		mV	mV	mV	
6.82	30	0.313	platinum	7.8–13.2	22–100	–	this work
–	44	0.02	SCE	30	n.a.	180	[73]
–	43	1.13	zinc	<25	50	100	[70]
–	10	0.01–0.2	zinc	n.a.	n.a.	85–140	[74]
2	–	0.1	zinc wire	10	50	100	[75]
8.4	–	0.74	Hg/HgO	<25	50	75–200	[76]
1	–	0.1	Hg/HgO	30	90	130–220	[77]
1	–	0.1	Hg/HgO	20–30	n.a.	n.a.	[78]
7	–	0.7	Hg/HgO	≥ 17	n.a.	n.a.	[79]
4 and 6	–	0.1	zinc	<25	n.a.	n.a.	[80]
6.0	–	0.5	Hg/HgO	20	60–140	320	[71]
6	–	0.1–0.4	Hg/HgO	n.a.	30–80	n.a.	[81]
6	–	0.4	zinc wire	25	65	125–150	[82]
8	–	0.243	Hg/HgO	~21	~111	~258	[83]

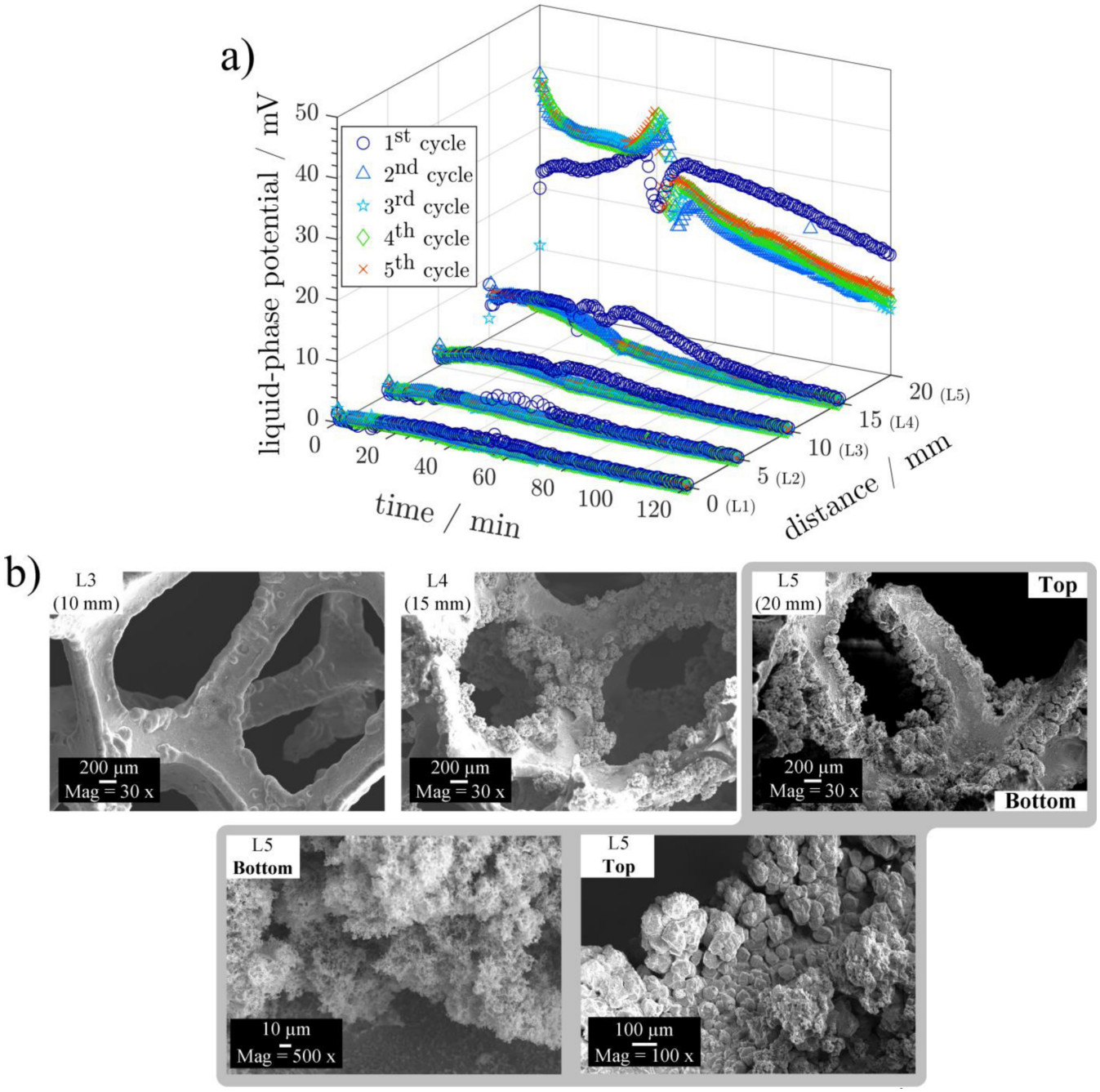

Figure 7. Conditions at a porous copper foam with a thickness (*z*-axis) of 20 mm during charging at 50 mA cm^{-2}. a) Potential distribution determined over five charge cycles at five liquid-phase potential probes (L1–L5) across the metal foam. The probes were spaced 5 mm apart. b) SEM images of the zinc structures near the probe tips of L3–L5 (10 mm–20 mm) formed in an additional charging process at 50 mA cm^{-2}. In addition, the zinc structures at the top and bottom region of the SEM image taken near the probe tip of L5 (20 mm) were examined at 100× and 500× magnification.

50 mA cm^{-2} differ significantly, with the highest potential in all five charging processes measured each time at probe L5 (20 mm). This finding was expected due to the known heterogeneous potential distribution within the foam and the associated high zinc deposition near the counter electrode (Figure 5). When comparing the potential signals, it is noticeable that the one of the 1st cycle always showed higher values, except for probe L5 (20 mm) at the beginning of the charging process. In contrast, in the repeated experiment (Figure S3f–j) and in further experiments at a current density of 130 mA cm^{-2} (Figure S8a–j) the measured probe potentials at L5 (20 mm) were always higher during the 1st cycle than in all subsequent charging processes. This is likely due to the initial zinc nucleation over a pristine copper substrate. The reason for the deviation during the 1st charging cycle in Figure 7a might be due to a shading of the probe tip by residual gas bubbles in the system.

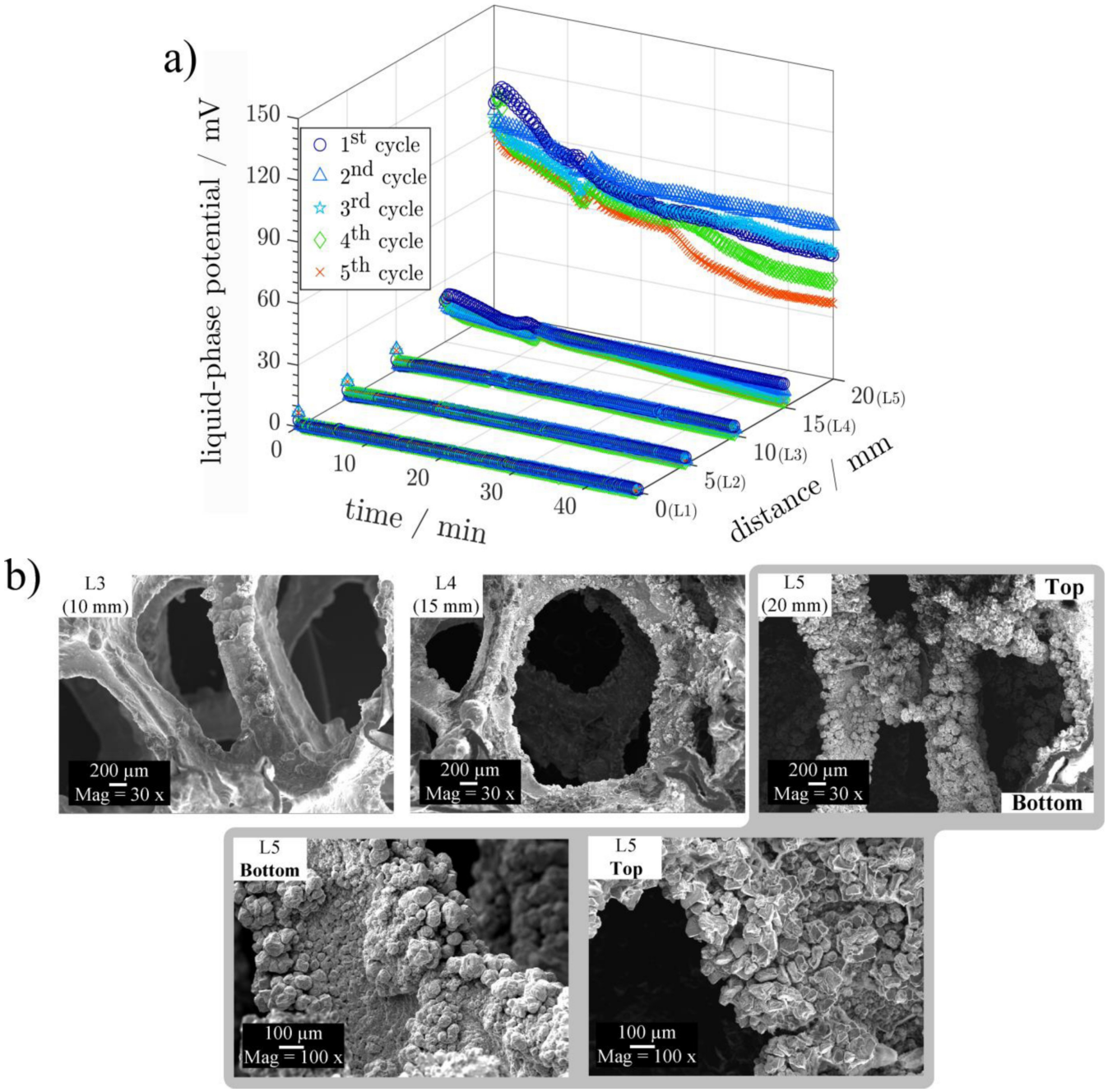

Figure 8. Utilization of a porous copper foam with a thickness (*z*-axis) of 20 mm during charging at 130 mA cm^{-2}. a) Potential distribution determined over five charge cycles at five liquid-phase potential probes (L1–L5) across the metal foam. The probes were spaced 5 mm apart. b) SEM images of the zinc structures near the probe tips of L3–L5 (10 mm–20 mm) formed in an additional charging process at 130 mA cm^{-2}. In addition, the zinc structures at the top and bottom region of the SEM image taken near the probe tip of L5 (20 mm) were examined at 100× magnification.

Another similarity among the measurements in Figure 7a is the decrease of the potential from the beginning to the end of the experiment. This is particularly noticeable for probes L3–L5 (10 mm–20 mm). This could be also observed at higher current densities of 90 mA cm^{-2} and 130 mA cm^{-2} (Figure S5a and Figure 8a). The reason for this is most likely the decrease in local current density caused by the increase in the surface area of the metal foam due to the formation of zinc structures as the deposition progresses.[70,71] Another noticeable characteristic of the recorded potentials is the occurrence of strong variations with steep gradients at a time range from 30 min to 50 min at a current density of 50 mA cm^{-2} (Figure 7a), which are particularly recognizable at probes L4 and L5. These measurement artifacts were also observed in the experiments with higher current densities of 90 mA cm^{-2} and 130 mA cm^{-2} (Figure S5a and Figure 8a). The occurrence and cause for these artifacts will be explained in detail in the following section but here it can be

said that it is not unexpected, being part of the ZASH flow battery voltage curve as reported in our previous work.[17]

The liquid-phase potentials measured with the probes L1—L3 (0 mm–10 mm) were 3 mV or less during all five charging cycles at a current density of 50 mA cm^{-2} (Figure 7a). The SEM image (Figure 7b) of the foam near the probe tip of L3 (10 mm) shows no remarkable changes of the pores and foam struts, which supports the earlier observation (Figure 5) that zinc deposition at and below 10 mm (z-axis) is vanishingly small. Negligible or small amounts of reduced metal close to the current collector are typical and clearly observed in other flow cell studies deliberately using thick porous electrodes, such as for platinum reduction on titanium felt and mesh.[32,72]

The potentials measured with the probes L4 (15 mm) and L5 (20 mm) were 7.8 mV and 39.0 mV at the beginning of the 5th charging process at a current density of 50 mA cm^{-2}. After 120 min at the end of the experiment, the potentials decreased to 0 mV and 13.2 mV, respectively. The SEM image of the foam at the position of the probe tip of L4 shows the characteristic properties of the moss-like zinc structures (Figure 7b). In fact, the measured potential of 7.8 mV at the beginning of the experiment is quite close to the potential range of 10 mV to 30 mV (Table 1) and thus the formation of mossy structures was expected during charging. In contrast, the initially measured overpotentials above 30 mV at probe tip L5 (20 mm) during the charging indicate the formation of the preferred boulder structures. Indeed, the zinc deposits examined exhibited a boulder-like morphology in the top region of the SEM image in Figure 7b. However, as can be seen in Figure S4, the steady decrease of the potential to 13.2 mV at the end of charging, resulted in the onset growth of moss-like structures on top of the initially formed boulder structures. Furthermore, the bottom region of the SEM image near L5 (20 mm) (Figure 7b) shows already a growth of moss-like structures.

Similarities in the distribution of the zinc structures across the foam were found by comparing the experiments conducted at the current densities of 50 mA cm^{-2} and 90 mA cm^{-2}. Moss-like structures could also be detected near the probe tip of L4 (15 mm) after the charging process at 90 mA cm^{-2} (Figure S5b). The measured liquid-phase potentials had its maximum near 10 mV during the first 20 min of the five charging processes and were thus within the specified range of 10 mV to 30 mV for mossy zinc deposits (Table 1). The examined structures near the probe tip of L5 (20 mm) in the top region of the SEM image shows the desired boulder structure (Figure S5b). The measured probe potentials were in a range of 40 mV to 75 mV during the whole experiment and thus above the critical value of 30 mV reported for boulder-like structures in literature (Table 1). However, the repeated experiment (Figure S7f–j) shows that the potential can even fall below 20 mV at the end of charging (t = 120 min) and thus the formation of mossy structures cannot be prevented. A magnification of the bottom region of the SEM image in Figure S5b taken near the tip of L5 (20 mm) (Figure S6) confirms the growth of the moss-like structures on the top of the boulder structures. Consequently, a further charging would lead to a further decrease of the local liquid-phase potential and inevitably lead to overgrowth of the boulder-like structures even in the immediate vicinity of the probe tip of L5 (20 mm).

When the flow battery is operated at a current density of 130 mA cm^{-2}, zinc morphologies and their distribution across the thickness of the metal foam changes in comparison to the experiments at lower current densities. Accordingly, some mossy zinc deposits could be observed in the region of the probe tip of L3 (10 mm) at a probe potential of about 4 mV (Figure 8b and Figure S10a). Liquid-phase potentials of about 22 mV and 3 mV were measured at the probe tip of L4 (15 mm) at the beginning and end of the 5th charging process, respectively. The probe potential of 22 mV is below the critical value of 30 mV for the formation of boulder-like structures and thus the formation of mossy-like deposits is preferred (Table 1). Indeed, mossy structures are visible on the SEM image (Figure 8b), recognizable by the light gray colored deposits. However, a magnified region of these deposits (Figure S10b) reveals that small boulder structures are also present beneath the mossy deposits. As a result, boulder structures may already occur below the critical value of 30 mV reported in literature.

The deposits near the probe tip of L5 (20 mm) after charging at a current density of 130 mA cm^{-2} had, without any exception, the characteristics of boulder structures (Figure 8b). This is accompanied by the measured potentials of about 90 mV and 37 mV at the beginning and end of the 5th charge cycle, respectively, which are clearly within the potential range for the formation of boulder-like structures. However, there are slight differences in the shape of the deposits. A magnified SEM image of the bottom area near the position of L5 (20 mm) shows a sphere-like structure, whereas the deposits in the immediate vicinity of the probe tip in the top region show sharper edges. It is likely that at higher overpotentials caused by a current density over 130 mA cm^{-2} the deposits would become more sharp-edged and dendritic.

The repeated experiment (Figure S8f–j) at 130 mA cm^{-2} shows significantly higher overpotentials at probe L5 (20 mm) compared to the previous experiment (Figure 8a). Accordingly, the probe potentials measured at the beginning and at the end of the 5th charge cycle are 115 mV and 74 mV, respectively. Despite the high overpotentials, an SEM image of the foam pore near the probe tip of L5 (20 mm) (Figure S10c) shows that zinc structures similar to those in Figure 8b of the previous experiment are present at a current density of 130 mA cm^{-2}. The reason for the differences in the overpotential may be due to the probe tip shifting into a lower region of the metal foam during assembly in the previous experiment (Figure 8). The measured liquid-phase potential was about 100 mV during the first 20 min of charging and thus is defined as the upper limit of the potential range for the formation of boulder-like structures in this study (Table 1).

Despite the good agreement of the measured potentials and the zinc structures described above, the potential curves differ slightly from cycle to cycle in all experiments for both low and high current densities (Figure 7a, Figure S5a and Figure 8a). The most likely reason is the influence of the complex mechanisms at the positive GDE surface affecting the electric field at the negative electrode and thus the activity of the metal

foam during the charging cycle, as observed in our previous study.[17] At a current density of 130 mA cm^{-2}, the measured potentials actually decrease with each charge cycle, instead of stabilizing after a few cycles as they do at current densities of 50 mA cm^{-2} and 90 mA cm^{-2}. This phenomenon also causes the liquid-phase potential measured at probe L5 to be lower at the end of charging at 130 mA cm^{-2} than at 90 mA cm^{-2} (Figure 8a and Figure S5a). The reason for this could be the ageing onset of the GDE, which is accelerated by the high peak current and can lead to less active regions on the GDE and thus also on the opposite foam electrode. Consequently, the liquid-phase potential decreases with time.

Measurement Artifact and its Origin

As mentioned in a previous section, a measurement artefact is recognizable in the responses of the potential probes at the negative foam electrode during the charging process in the first half of all experiments, independently from the applied current density (Figure 7a, Figure S5a and Figure 8a). This is visible in particular in the potential measured with probes L4 and L5. The assumption from previous work is that the oxidation processes of the silver species in the GDE are the reason for this occurrence.[17] In order to examine this hypothesis, we replaced the GDE with a pure zinc plate (Grillo-Werke, Germany) after finishing an experiment with five charge-discharge cycles at a current density of 50 mA cm^{-2} (Figure 7a). Beyond that, no other cell components were replaced. After reassembling the flow cell, the experiment was started with the same charging procedure used during the previous experiment at 50 mA cm^{-2}.

As seen in Figure 9a, the cell potential measured during the 5th charging cycle using a GDE as a positive electrode corresponds to the typical potential curve of a ZASH flow battery reported in our previous study.[17] The encircled number 2 and the corresponding gray dashed line identify the potential peak at about 2.21 V (t = 41.35 min), which represents the transition from the highly-resistive silver(I)-oxide (ρ = 7×10^8 Ω cm)[84] to silver(II)-oxide (ρ = 5×10^3 Ω cm)[84] at the GDE.[17] The numbers 1 and 3 correspond to operating states six minutes before (t = 35.35 min) and after (t = 47.35 min) the peak occurs. In contrast, neither a potential shift to higher values nor a potential peak occurred when a zinc plate was used as the positive electrode. The overpotentials at the flow cell during the current pulse showed a constant value over time with a small decrease. The low cell voltage with a maximum of about

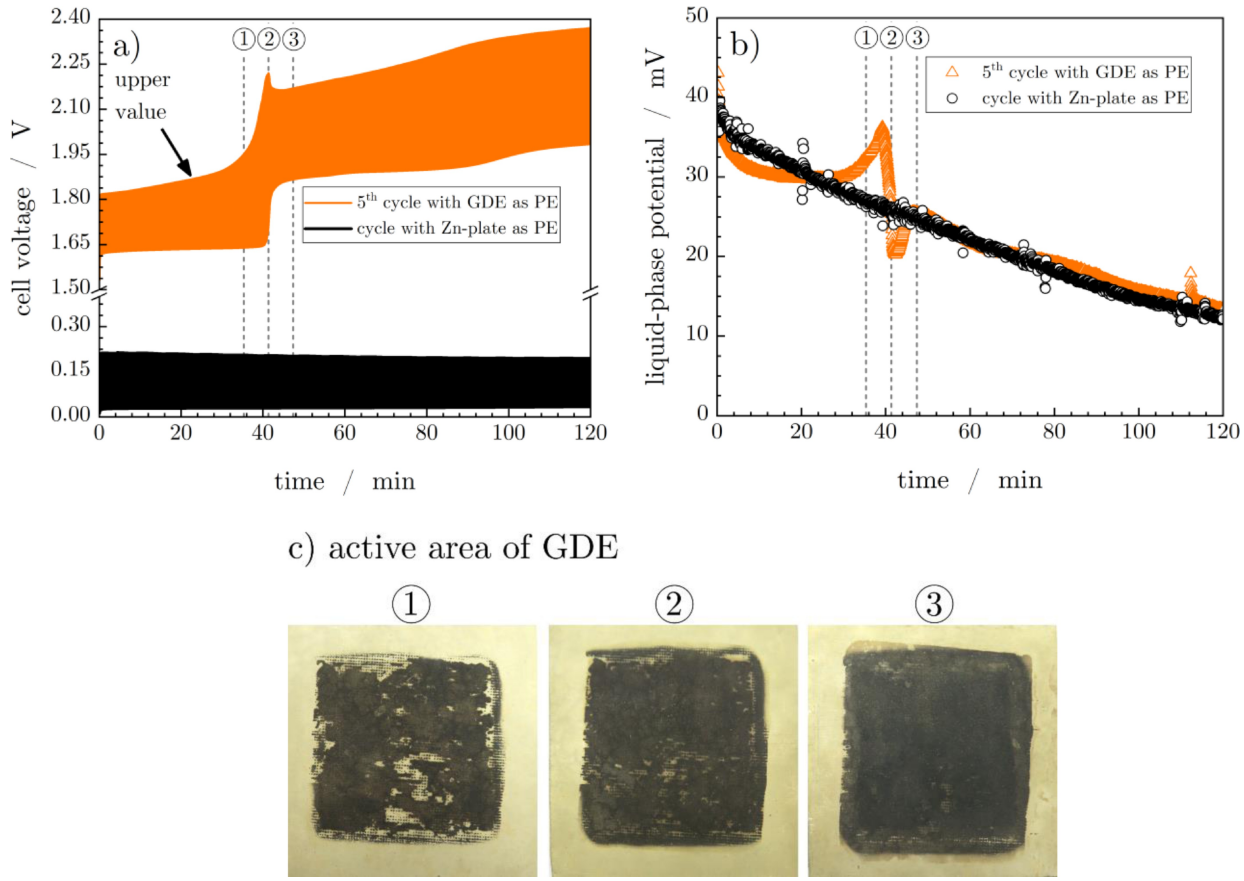

Figure 9. Evaluation of the impact of the GDE on the probe potentials measured inside the porous metal foam during charging at a current density of 50 mA cm^{-2}. a) Potentials during a charging cycle with a GDE as PE and an additional charging cycle with a Zn-plate as PE. The circled numbers from 1 to 3 denote crucial changes in the potential when using a GDE as a PE, caused by the different oxidation states of the silver in the GDE. Orange area represents the current range of the pulsed current regime. b) Probe potentials measured at the liquid-phase potential probe L5 (20 mm) using a GDE as PE and a Zn-plate as PE. c) Changes in the oxidation states of the active area of the GDE during charging.

0.2 V during a current peak is due to the fact that both electrodes are coated with or consist of zinc. In addition, the cell voltage does not drop to the expected 0 V during the current pause, which is most likely due to residual capacitance at the electrodes.

The liquid-phase potentials during the charging processes were measured at probe L5 (20 mm) and are shown in Figure 9b. For comparison, the predefined time frame from Figure 9a is also shown, indicated by the encircled numbers from 1 to 3. The potential curve of the 5th charge cycle with a GDE as PE shows the expected measurement artifact occurring within the same time frame. In contrast, no artifact was observed when a zinc plate is used as PE, which is consistent with the observations already made in Figure 9a. This finding indeed confirms that the measurement artifact is most likely attributable to the oxidation processes of the silver species at the GDE. Apart from this, however, the measured potentials before and after the occurrence of the artifact correspond to those measured with a zinc plate as PE (Figure 9b).

In further experiments, different oxidation states of the GDE were examined to determine possible correlations between the probed potential and the measurement artifact encountered. Therefore, the battery cell was again operated at a current density of 50 mA cm^{-2} and charged differentially up to the operating states indicated by the encircled numbers 1 to 3 in Figure 9a, b. The flow cell was subsequently disassembled in each case, and the active area of the GDE was examined qualitatively with photography. As seen in Figure 9c, the oxidation of the active area of the GDE was heterogeneous up to the operating state 1 (t = 35.35 min). The brownish spots indicate that oxidized silver species are already present. In contrast, the brighter and smaller spots correspond to the non-oxidized silver species in the electrode matrix. As can be seen in Figure 9b, the measured probe potential at probe tip L5 increased before and after reaching the operating state 1. Several factors, such as electrolyte concentration, the distance of the probe tip to the metal foam pore and the conductivity of the electrolyte or electrode, could cause this rise in the potential. However, these factors do not change over time to the extent that the potential would shift to remarkably higher values. More likely is the increase of the local current density, which is caused by the preferred current flow through the non-oxidized areas at the GDE instead of the areas containing highly resistive silver oxides. As a result, the local current density is higher in the areas without oxides, leading to higher potentials and, thus higher activity at the parallel metal foam near these areas.

When operating the flow cell up to the potential peak at the operating state 2 (t = 41.35 min) in Figure 9a, the bright non-oxidized areas almost completely disappeared (Figure 9c). This is consistent with the fact described in the literature that at this point, the silver species have been completely converted to silver(I)-oxide and further oxidation to silver(II)-oxide is initiated.[17,84–86] Extending the test time by further six minutes leads to the operating state 3 (t = 47.35 min) (Figure 9a) and results in a complete coverage of the active area of the GDE with silver oxides. The appearance of the area changed to a darker color compared to the area at the potential peak and is most likely due to oxidation of the silver species. The cell voltage decrease between the operating states 2 and 3 (Figure 9a) is due to oxidation to a low-resistance silver(II)-oxide layer on the GDE surface. The decrease is also recognizable in the curve of the probe potential in Figure 9b. This is probably due to an equalization of the current distribution in the active region of the GDE caused by the progressive oxidation and disappearance of heterogeneous areas with non-oxidized silver species. As a result, the hotspots of high local current densities disappear and so does the increased activity at the metal foam.

Ohmic Contribution to the Potentials Measured in Liquid-Phase

As described in the experimental section, CI measurements were conducted every 30 s during the charging process. The resulting *iR* drop values include several ohmic potential losses mainly caused by the properties of the cell components, such as the conductivity of the electrolyte and electrode materials.[87] Additionally, passive layers at the electrode surfaces may increase the *iR* drop. However, the effects of possible passive layers on the zinc electrode are negligible since they form preferentially during the discharge process.[5,88]

CI measurements were performed with the potential probes L3–L5 (10 mm–20 mm) at current densities of 50 mA cm^{-2}, 90 mA cm^{-2} and 130 mA cm^{-2} (Figure 10, Figure S11a, b, Figure S12a, b, c and Figure S13a, b, c). However, in the following, only the results of the measurement carried out at a current density of 50 mA cm^{-2} with the potential probe L5 (20 mm) are discussed. This is due to the fact that the results of the tests at higher current densities are similar and differ only in the magnitude of the probe potentials. This also applies to the potentials measured with probes L3 (10 mm) and L4 (15 mm).

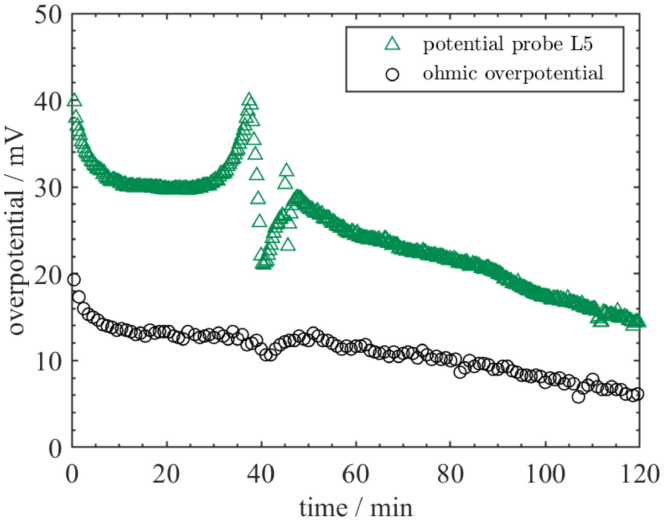

Figure 10. Potential measured at the liquid-phase potential probe L5 (20 mm) during a charging process at 50 mA cm^{-2} alongside the ohmic overpotential determined from CI measurements taken every 30 s during the same charging step.

The CI measurements were repeated with replaced cell components and different potential probes. The results are similar to those of the previous experiments (Figure S11c, d, Figure S12d, e, f and Figure S13d, e, f).

As shown in Figure 10, the ohmic overpotential between the probe tip at L5 (20 mm) and the metal foam was about 20 mV at the beginning of the charging process at a current density of 50 mA cm^{-2}. This value corresponds to about 50 % of the overall measured liquid-phase potential at probe L5 at the beginning. The previously mentioned measurement artifact due to the presence of the silver-based GDE is clearly visible in the curve of the probe potential during the experimental period of 30 min to 50 min. Besides slight changes in the potentials around 40 min, no other potential gradients are visible in the curve of the ohmic overpotential. This result is similar to the results of the CI measurements at the current densities of 90 mA cm^{-2} and 130 mA cm^{-2} (Figure S12a and Figure S13a), although the slight decrease in the ohmic overvoltage curve mentioned above is more pronounced.

It seems that the conversion processes of silver at the GDE surface already have a minor impact on the *iR* drop at the metal foam. Apart from the fact that the used sampling rate of 100 µs is too low, possible influences on the course of the ohmic overpotential are given in the following. According to Ohm's law, the resistance and the applied current determine the magnitude of the ohmic overpotential at the electrode. However, the resistances caused by the electrolyte and the electrode material are expected to be almost constant during charging. Accordingly, the conductivity of the electrolyte used, consisting of a 30 wt % KOH solution and 2 wt % dissolved ZnO, changed only slightly from ~605 mS cm^{-1} ($Q = 0$ Ah) to ~610 mS cm^{-1} ($Q = 1200$ Ah) during a typical charging process. Furthermore, the overpotential at the metal foam is negligible throughout the charging process (Figure 6). Indeed, the conductivity of copper (~58.0×10^6 S m^{-1}) is higher than the one of the deposited zinc (~16.7×10^6 S m^{-1}), but the value is by far higher than the conductivity of the electrolyte and thus the impact on the ohmic overpotential is negligible. Consequently, the most likely reason for the potential changes in the ohmic overpotential is the already discussed reduction in current caused by the different local oxidation states of the GDE surface. Complex experiments would be needed to fully understand the mechanism of the measurement artifact and the influence of the GDE on the measured probe potentials at the metal foam.

At the end of the charging process ($t = 120$ min) the ohmic overpotential and the probe potential at L5 (20 mm) decreased to about 6 mV and 14 mV (Figure 10), respectively. This decrease was expected since the formation of zinc structures lead to an increase of the surface area and thus to a decrease in local current density as described in a previous section.

Liquid-Phase Potentials During Discharging

Figure 11 shows the potentials measured at the quasi-reference probe tips of L1–L5 (0 mm–20 mm) in the negative metal foam electrode during discharge at a constant current density of 50 mA cm^{-2}. The corresponding charging steps were performed at a current density of 50 mA cm^{-2} and are displayed in Figure 7a. Since all discharge tests were conducted at the same current density regardless of the current density applied during the charging process, the following discussion is based on the results shown in Figure 11. Indeed, a comparison of the potentials measured during discharge after charging at a current density of 50 mA cm^{-2} and 130 mA cm^{-2} shows no significant differences (Figure S14a–j). The punctual potential drops that occurred during some discharge cycles, seen in particular in Figure S14g at probe L2, were likely caused by the passing of bubbles between the probe tip and the metal foam.

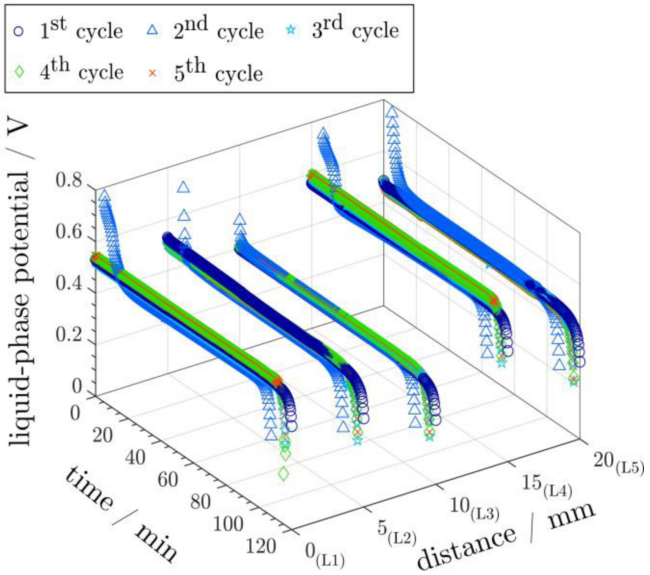

Figure 11. Potential distribution measured using five liquid-phase potential probes (L1–L5) within a metal foam with a thickness (*z*-axis) of 20 mm during discharge at 50 mA cm^{-2}. The corresponding charging cycles were conducted at a current density of 50 mA cm^{-2} (Figure 7a).

The discharge graphs displayed in Figure 11 show similar trends regardless of the probe location and cycle number. In contrast to the dependency of liquid-phase potential on the electrode thickness during charging (zinc reduction), no clear relationship between the same potentials and distance is observed during discharging (zinc oxidation). This may be due to the fact that the discharge constant current is lower than the pulsed current applied during charging, implying lower overpotentials and a less intense potential distribution across the electrode. Plus, zinc oxidation takes place from a wholly covered zinc surface. Only the 2nd discharge cycle showed an increased potential at the beginning of the experiment and a shortened test duration, which is almost the same for all probes. The reasons for this are unclear but it is likely due to a local disturbance at the GDE caused by partial drying out or screening of the active area due to a gas bubble lodged between the separator and GDE during charging. However, subsequent discharge cycles did not exhibit any of these irregularities, so this will not be discussed further.

The measured potential at the beginning of discharging differs from probe to probe in a range of 0.4 V to 0.6 V, which is probably due to slight differences in the probes and their surrounding environment. Small impurities on the probe tip caused by the challenging integration of the probes into the foam pores during cell assembly or by the flow battery operation itself may have some impact on the probe potential. Apart from these minor differences in the recorded potentials, no measurement artifacts, such as those occurring during the charging processes, are visible. This finding is remarkable because a change in the oxidation states of silver also takes place at the positive GDE during discharge.[17,85,89] Presumably, the reduction of the silver oxides proceeds more uniformly than the oxidation during the charging process. This could be explained by the low constant current that is supplied during discharge, which is only one-third of the peak pulsed current during charge. A lower current means lower overpotentials and a slower reaction rate at the silver species in the GDE. More details could be obtained by discharging the cell to various operating states and then disassembling it to study the GDE, as was done in the charging process (Figure 9c). Finally, at the end of the discharge processes, a steep potential drop towards 0 V can be seen, which is caused by zinc depletion on the metal foam, i.e., full discharge of the cell.

Conclusions

In this study, we have successfully integrated liquid-phase and solid-phase potential probes into a porous copper foam serving as the substrate for the negative electrode of a ZASH flow battery. This allowed us to determine the potential distribution across the thickness of the metal foam during the operation of the flow battery. We validated a quasi-reference electrode against DHEs with various resistances and a Hg/HgO electrode. The simple quasi-reference probes showed superior stability in a zinc-containing electrolyte and were thus used in the flow cell experiments. Our investigation demonstrated that the measured potential at the liquid-phase potential probes directly reflects the local electrode overpotentials. Our findings align well with prior knowledge of potential distribution at foam electrodes in rectangular channel flow cells (e.g.[27]), confirming that the magnitude of the local current is a function of distance from the current collector due to local overpotentials. In contrast, even at a relatively high pulsed current density of 130 mA cm^{-2} (390 mA cm^{-2} at pulse peak), the solid-phase exhibited negligible overpotentials, irrespective of its position in the foam electrode. We have also shown that local potentials control the formation of particular zinc morphologies on the metal foam as a function of distance from the current collector. Specifically, we identified moss-like structures within the overpotential range of 7.8 mV–13.2 mV and boulder-like structures within a range of 22 mV–100 mV. As in previous work,[17] we did not observe the formation of dendritic structures near the probe tips owing to the use of a pulsed charge regime during the charging steps. One noteworthy remark pertains to a measurement artifact observed at the negative electrode during the initial half of the charging steps, particularly in the potential curves measured with the probes near the positive GDE. Our subsequent experiments, replacing the silver containing GDE with a zinc plate, led to identifying the origin of this artifact, confirming the change of oxidation state of silver in the GDE as its source. However, the primary and most significant finding of our study is that, regardless of the applied current density, the region of highest activity for zinc deposition is concentrated near the GDE. Consequently, only the foremost 5 mm of the 20 mm thick copper metal foam is effectively utilized for zinc deposition, while the remaining 15 mm is thinly covered with zinc. Attempts to increase the flow battery capacity by choosing a metal foam thicker than approximately 5 mm are unlikely to provide significant benefits because the areas near the negative electrode current collector are not adequately utilized. This conclusion is relevant to similar electrochemical devices incorporating metal deposition on foam-structured electrodes.

Experimental

Cell Design and Potential Probes

An exploded view of the flow cell and a schematic diagram of a DHE liquid-phase potential probe are shown in Figure 1a, b. The cell design was based on the battery cell described in our previous work,[17] differing in dimensions and a reduced number of components. Due to the similarities, the description of the cell used here is focused on the modifications. The porous copper foam (average pore diameter ≈2 mm, volumetric porosity: 96.3 %) used as negative electrode substrate, had a geometric area of 12 cm^2, a thickness of 20 mm and was provided by Xiamen Zopin, China. The porosity was calculated from the bulk density of a foam sample of known volume. The inlet and outlet of the electrolyte were located at the top of the electrode frame. The flow direction of the electrolyte is not from bottom to top, as in our previous study,[17] but from right to left (Figure 2b). To meet the requirement of a similar flow regime and thus comparability of the results of both studies, the foam orientation was rotated by 90° to the current collector. A further modification of the flow cell design is the integration of the flow field directly on the air supply frame, which simplifies the assembly.

All experiments were performed with an aqueous alkaline electrolyte consisting of 30 wt % KOH (pellets, 85 % purity, VWR Chemicals) and 2 wt % dissolved ZnO (powder, 99 % purity, Grillo-Werke, Germany). The electrolyte flow rate was set to 500 mL min^{-1} (≈1.04 cm s^{-1} interstitial flow velocity through the foam) with the help of a peristaltic pump (323 U, Watson Marlow, USA). An electrolyte volume of 1.0 L was circulated between the cell and a separate tank. After each experiment, the electrolyte was completely replaced to enable the same initial conditions. The electrolyte tank was constantly flushed with nitrogen (5.0 grade, Linde) to prevent carbonate formation in the solution through the absorption of carbon dioxide from ambient air. Synthetic air (5.0 grade, Linde) was supplied with a flow rate of 0.5 L h^{-1} as reaction gas to the bifunctional GDE sourced from Covestro, Germany. Both gases, nitrogen and synthetic air, were humidified in wash bottles to prevent water removal from the electrolyte.

Electrochemical and Optical Characterizations

The flow cell experiments and the stability tests were performed using a Reference 3000AE potentiostat coupled to a Reference [30k] Booster (Gamry Instruments, USA) for enabling currents above 3 A. The flow cell tests with integrated potentials probes consisted of five charge-discharge cycles and one additional cycle with repeated CI measurements during charging and a subsequent charging process. The latter was used for post-mortem examination of the zinc structures deposited on the metal foam. The charging was realized by a pulsed charging protocol adapted from our previous study with a pulse-pause ratio of 1 s to 2 s.[17] When evaluating the data, the liquid-phase and solid-phase potentials were calculated as the difference between the potentials measured at the end of a pause at 2 s and at the subsequent end of the pulse at 1 s. The transferred capacity during charging steps was limited to 1.2 Ah. In three series of tests performed, current densities of 50 mA cm^{-2}, 90 mA cm^{-2} and 130 mA cm^{-2} were applied during charging with respect to the geometric area of the foam (12 cm^2). Taking into account the above pulse-pause-ratio, peak current densities had values of 150 mA cm^{-2}, 270 mA cm^{-2} and 390 mA cm^{-2}.[17]

The discharge of the ZASH's single cell was performed in accordance with our previous study at a constant current density of 50 mA cm^{-2} until reaching a cut-off voltage of 0.9 V.[17] This limit is crucial to prevent oxidation of the tin coating of the current collector. The applied CI method was adapted from our previous study.[17] A CI measurement was taken every 30 seconds during the charging process. Here, the same current as during the charging process was applied for 1 ms, followed by a switch-off time of 1 ms. The sampling rate was 100 µs. A high-performance scanning electron microscope (SEM) (EVO 50 MA 10, ZEISS, Germany) was used to examine the morphology of zinc deposits. For this purpose, the foam samples were cut along the *xz*-plane (Figure 2a) at a height (*y*-axis) of 20 mm, where the tips of the liquid-phase potential probes were located during the experiments. This allowed a direct correlation of the zinc structures with the measured overpotentials in the liquid-phase.

Supporting Information

Supporting Information is available from the Wiley Online Library or from the author.

Acknowledgements

This work was supported by the German Federal Ministry of Education and Research (BMBF) under the ZiLsicher project (grant number 03XP0191B). L. F. A. is grateful to the Alexander von Humboldt Foundation (Germany) for sponsoring a research fellowship at Clausthal University of Technology. The authors also thank Mr. Lars H. Sanderbrandes for his dedicated support during his M.Sc. thesis work. Open Access funding enabled and organized by Projekt DEAL.

Conflict of Interests

The authors declare no conflict of interest.

Data Availability Statement

The data that support the findings of this study are available from the corresponding author upon reasonable request.

Keywords: porous metal foam · potential probe · zinc morphology · liquid-phase potential · solid-phase potential

[1] E. T. Sayed, A. G. Olabi, A. H. Alami, A. Radwan, A. Mdallal, A. Rezk, M. A. Abdelkareem, *Energies* **2023**, *16*, 1415.
[2] M. Krichen, Y. Basheer, S. M. Qaisar, A. Waqar, *Energies* **2023**, *16*, 2271.
[3] N. Borchers, S. Clark, B. Horstmann, K. Jayasayee, M. Juel, P. Stevens, *J. Power Sources* **2021**, *484*, 229309.
[4] J. Fu, R. Liang, G. Liu, A. Yu, Z. Bai, L. Yang, Z. Chen, *Adv. Mater.* **2019**, *31*, e1805230.
[5] S. Yang, H. Du, Y. Li, X. Wu, B. Xiao, Z. He, Q. Zhang, X. Wu, *Green Energy & Environ.* **2022**, *8*, 1531–1552.
[6] L. F. Arenas, A. Loh, D. P. Trudgeon, X. Li, C. Ponce de León, F. C. Walsh, *Renewable Sustainable Energy Rev.* **2018**, *90*, 992–1016.
[7] K. W. Leong, Y. Wang, M. Ni, W. Pan, S. Luo, D. Y. Leung, *Renewable Sustainable Energy Rev.* **2022**, *154*, 111771.
[8] J. Yi, P. Liang, X. Liu, K. Wu, Y. Liu, Y. Wang, Y. Xia, J. Zhang, *Energy Environ. Sci.* **2018**, *11*, 3075–3095.
[9] L. Miao, J. Zhang, Y. Lv, L. Gan, M. Liu, *Chemistry* **2023**, *29*, e202203973.
[10] S. Kolhekar, M. Nyce, S. Banerjee, *J. Electrochem. Soc.* **2021**, *168*, 40514.
[11] Z. Yan, E. Wang, L. Jiang, G. Sun, *RSC Adv.* **2015**, *5*, 83781–83787.
[12] Z. Kang, C. Wu, L. Dong, W. Liu, J. Mou, J. Zhang, Z. Chang, B. Jiang, G. Wang, F. Kang et al., *ACS Sustainable Chem. Eng.* **2019**, *7*, 3364–3371.
[13] J. Yu, F. Chen, Q. Tang, T. T. Gebremariam, J. Wang, X. Gong, X. Wang, *ACS Appl. Nano Mater.* **2019**, *2*, 2679–2688.
[14] X. Shi, G. Xu, S. Liang, C. Li, S. Guo, X. Xie, X. Ma, J. Zhou, *ACS Sustainable Chem. Eng.* **2019**, *7*, 17737–17746.
[15] C. Li, X. Shi, S. Liang, X. Ma, M. Han, X. Wu, J. Zhou, *Chem. Eng. J.* **2020**, *379*, 122248.
[16] M. Bockelmann, U. Kunz, T. Turek, *Electrochem. Commun.* **2016**, *69*, 24–27.
[17] S. Genthe, L. F. Arenas, U. Kunz, T. Turek, *Energy Technol.* **2023**, *11*, 2300552.
[18] J. S. Ko, K. Bishop, N. Seitzman, B.-R. Chen, M. F. Toney, J. Nelson Weker, *J. Electrochem. Soc.* **2020**, *167*, 140520.
[19] A. R. Mainar, L. C. Colmenares, J. A. Blázquez, I. Urdampilleta, *Int. J. Energy Res.* **2018**, *42*, 903–918.
[20] J. S. Newman, C. W. Tobias, *J. Electrochem. Soc.* **1962**, *109*, 1183.
[21] J. J. Coleman, *J. Electrochem. Soc.* **1951**, *98*, 26.
[22] R. J. Brodd, *Electrochim. Acta* **1966**, *11*, 1107–1117.
[23] P. Bro, H. Y. Kong, *J. Electrochem. Soc.* **1971**, *118*, 519.
[24] Z. Nagy, J. O. Bockris, *J. Electrochem. Soc.* **1972**, *119*, 1129.
[25] M.-B. Liu, G. M. Cook, N. P. Yao, *J. Electrochem. Soc.* **1982**, *129*, 239–246.
[26] F. Leroux, F. Coeuret, *Electrochim. Acta* **1983**, *28*, 1857–1863.
[27] S. Langlois, F. Coeuret, *J. Appl. Electrochem.* **1990**, *20*, 740–748.
[28] J. L. Nava, M. T. Oropeza, C. Ponce de León, J. González-García, A. J. Frías-Ferrer, *Hydrometallurgy* **2008**, *91*, 98–103.
[29] A. I. Masliy, N. P. Poddubny, A. Medvedev, V. O. Lukyanov, *J. Electroanal. Chem.* **2015**, *757*, 128–136.
[30] T. Pérez, L. F. Arenas, D. Villalobos-Lara, N. Zhou, S. Wang, F. C. Walsh, J. L. Nava, C. Ponce de León, *J. Electroanal. Chem.* **2020**, *873*, 114359.
[31] X. Fu, J. Li, H. Zhang, J. Xian, *Int. J. Adv. Manuf. Technol.* **2022**, *121*, 1851–1866.
[32] L. F. Arenas, C. Ponce de León, R. P. Boardman, F. C. Walsh, *Electrochim. Acta* **2017**, *247*, 994–1005.
[33] A. L. Clemens, J. T. Davis, C. A. Orme, A. Ivanovskaya, R. Akolkar, N. A. Dudukovic, *J. Electrochem. Soc.* **2023**, *170*, 12502.
[34] X. Ma, Z. Jing, C. Feng, M. Qiao, D. Xu, *Renewable Sustainable Energy Rev.* **2023**, *173*, 113111.
[35] O. Lanzi, U. Landau, *J. Electrochem. Soc.* **1990**, *137*, 585–593.
[36] J. Andre, N. Guillet, J.-P. Petit, L. Antoni, *J. Fuel Cell Sci. Technol.* **2010**, *7*.
[37] C. Guzmán, A. Alvarez, S. Rivas, S. M. Durón-Torres, A. U. Chávez-Ramírez, J. Ledesma-Garcia, L. G. Arriaga, *Int. J. Electrochem. Sci.* **2013**, *8*, 8893–8904.
[38] Q. Liu, A. Turhan, T. A. Zawodzinski, M. M. Mench, *Chem. Commun. (Camb.)* **2013**, *49*, 6292–6294.

[39] C. Choi, Y. Choi, S. Kim, H. Jung, H.-T. Kim, *Electrochim. Acta* **2016**, *213*, 490–495.
[40] Y. A. Gandomi, D. S. Aaron, T. A. Zawodzinski, M. M. Mench, *J. Electrochem. Soc.* **2016**, *163*, A5188–A5201.
[41] A. Appleby, G. Crepy, J. Jacquelin, *Int. J. Hydrogen Energy* **1978**, *3*, 21–37.
[42] C. Pitti, M. Herlem, *Anal. Lett.* **1979**, *12*, 439–444.
[43] J. Giner, *J. Electrochem. Soc.* **1964**, *111*, 376.
[44] H. Binder, A. Köhling, G. Sandstede, *Chem. Ing. Tech.* **1971**, *43*, 1084–1088.
[45] S. Kim, J. Yan, B. Schwenzer, J. Zhang, L. Li, J. Liu, Z. Yang, M. A. Hickner, *Electrochem. Commun.* **2010**, *12*, 1650–1653.
[46] C. Choi, S. Kim, R. Kim, J. Lee, J. Heo, H.-T. Kim, *J. Ind. Eng. Chem.* **2019**, *70*, 355–362.
[47] A. Küver, I. Vogel, W. Vielstich, *J. Power Sources* **1994**, *52*, 77–80.
[48] G. Li, P. G. Pickup, *Electrochim. Acta* **2004**, *49*, 4119–4126.
[49] Z. Siroma, R. Kakitsubo, N. Fujiwara, T. Ioroi, S.-I. Yamazaki, K. Yasuda, *J. Power Sources* **2006**, *156*, 284–287.
[50] M. Carmo, T. Roepke, F. Scheiba, C. Roth, S. Moeller, H. Fuess, J. G. Poco, M. Linardi, *Mater. Res. Bull.* **2009**, *44*, 51–56.
[51] T. J. Smith, K. J. Stevenson in *Handbook of Electrochemistry*, Elsevier, **2007**, pp. 73–110.
[52] D. Alfisi, A. N. Shocron, R. Gloukhovski, D. A. Vermaas, M. E. Suss, *ACS Sustainable Chem. Eng.* **2022**, *10*, 12985–12992.
[53] T. Lemmermann, M. Becker, M. Stehle, M. Drache, S. Beuermann, M. S. Bogar, U. Gohs, U. E. Fittschen, T. Turek, U. Kunz, *J. Power Sources* **2022**, *533*, 231343.
[54] M. H. Chakrabarti, R. Dryfe, E. Roberts, *Electrochim. Acta* **2007**, *52*, 2189–2195.
[55] C. G. Armstrong, K. E. Toghill, *J. Power Sources* **2017**, *349*, 121–129.
[56] F. N. Büchi, G. G. Scherer, *J. Electrochem. Soc.* **2001**, *148*, A183.
[57] H. Kuhn, B. Andreaus, A. Wokaun, G. G. Scherer, *Electrochim. Acta* **2006**, *51*, 1622–1628.
[58] V. S. Bagotzky, E. I. Khrushcheva, M. R. Tarasevich, N. A. Shumilova, *J. Power Sources* **1982**, *8*, 301–309.
[59] S. Cherevko, A. R. Zeradjanin, G. P. Keeley, K. J. J. Mayrhofer, *J. Electrochem. Soc.* **2014**, *161*, H822–H830.
[60] Z. Wang, E. Tada, A. Nishikata, *J. Electrochem. Soc.* **2016**, *163*, C853–C855.
[61] M. Schalenbach, O. Kasian, M. Ledendecker, F. D. Speck, A. M. Mingers, K. J. J. Mayrhofer, S. Cherevko, *Electrocatalysis* **2018**, *9*, 153–161.
[62] R. M. Dell, D. A. J. Rand, *Understanding batteries*, Royal Society of Chemistry, Cambridge, **2001**.
[63] T. Nann, G. A. Urban, *Sens. Actuators B* **2000**, *70*, 188–195.
[64] J. Euler, W. Nonnenmacher, *Electrochim. Acta* **1960**, *2*, 268–286.
[65] J. Newman, W. Tiedemann, *AIChE J.* **1975**, *21*, 25–41.
[66] T. Doherty, J. G. Sunderland, E. Roberts, D. J. Pickett, *Electrochim. Acta* **1996**, *41*, 519–526.
[67] R. Khezri, S. Rezaei Motlagh, M. Etesami, A. A. Mohamad, F. Mahlendorf, A. Somwangthanaroj, S. Kheawhom, *Chem. Eng. J.* **2022**, *449*, 137796.
[68] J.-C. Riede, T. Turek, U. Kunz, *Electrochim. Acta* **2018**, *269*, 217–224.
[69] A. Khor, P. Leung, M. R. Mohamed, C. Flox, Q. Xu, L. An, R. Wills, J. R. Morante, A. A. Shah, *Mater. Today Energy* **2018**, *8*, 80–108.
[70] S. Arouete, K. F. Blurton, H. G. Oswin, *J. Electrochem. Soc.* **1969**, *116*, 166.
[71] T. Otani, M. Nagata, Y. Fukunaka, T. Homma, *Electrochim. Acta* **2016**, *206*, 366–373.
[72] L. F. Arenas, C. Ponce de León, R. P. Boardman, F. C. Walsh, *J. Electrochem. Soc.* **2017**, *164*, D57–D66.
[73] J. Oxley, *The improvement of zinc electrodes for electrochemical cells.* Final Report, **1966**.
[74] J. W. Diggle, A. R. Despic, J. O. Bockris, *J. Electrochem. Soc.* **1969**, *116*, 1503.
[75] J. O. Bockris, Z. Nagy, D. Drazic, *J. Electrochem. Soc.* **1973**, *120*, 30.
[76] D.-T. Chin, R. Sethi, J. McBreen, *J. Electrochem. Soc.* **1982**, *129*, 2677–2685.
[77] M. Simicic, K. Popov, *J. Serb. Chem. Soc.* **2000**, *65*, 661–670.
[78] M. V. Simičić, K. I. Popov, N. V. Krstajić, *J. Electroanal. Chem.* **2000**, *484*, 18–23.
[79] R. Y. Wang, D. W. Kirk, G. X. Zhang, *ECS Trans.* **2007**, *2*, 19–27.
[80] N. Shaigan, W. Qu, T. Takeda, *ECS Trans.* **2010**, *28*, 35–44.
[81] W. Hong, Z. Jia, B. Wang, *J. Appl. Electrochem.* **2016**, *46*, 1085–1090.
[82] N. Nikolic, P. Zivkovic, G. Brankovic, M. Pavlovic, *J. Serb. Chem. Soc.* **2017**, *82*, 539–550.
[83] J. Dundálek, I. Šnajdr, O. Libánský, J. Vrána, J. Pocedič, P. Mazúr, J. Kosek, *J. Power Sources* **2017**, *372*, 221–226.
[84] B. D. Cahan, J. B. Ockerman, R. F. Amlie, P. Rüetschi, *J. Electrochem. Soc.* **1960**, *107*, 725.
[85] C.-C. Chang, Y.-C. Lee, H.-J. Liao, Y.-T. Kao, J.-Y. An, D.-Y. Wang, *ACS Sustainable Chem. Eng.* **2019**, *7*, 2860–2866.
[86] T. P. Dirkse, *J. Electrochem. Soc.* **1959**, *106*, 453.
[87] S. Anantharaj, S. Noda, *J. Mater. Chem. A* **2022**, *10*, 9348–9354.
[88] M. Bockelmann, M. Becker, L. Reining, U. Kunz, T. Turek, *J. Electrochem. Soc.* **2018**, *165*, A3048–A3055.
[89] P. Tan, B. Chen, H. Xu, W. Cai, W. He, H. Zhang, M. Liu, Z. Shao, M. Ni, *ACS Appl. Mater. Interfaces* **2018**, *10*, 36873–36881.

Manuscript received: January 22, 2024
Revised manuscript received: March 15, 2024
Version of record online: April 15, 2024

RESEARCH ARTICLE

Porous electrodes enhance mass transfer to a greater electrode surface area and improve fluid flow distribution of the electrolyte. Their use in flow batteries has therefore become increasingly important in recent years. The application of quasi-reference electrodes to a copper foam in a zinc-air/silver hybrid flow battery reveals a non-uniform utilization across the foam thickness with the highest activity near the counter electrode.

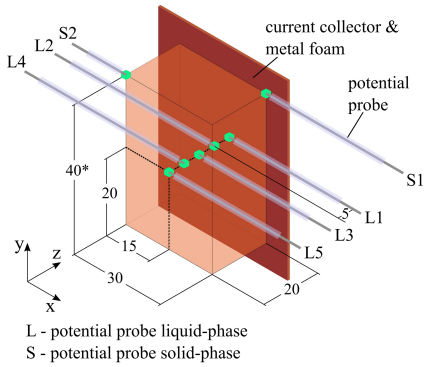

S. Genthe, Dr. L. F. Arenas, Dr. M. Becker, Prof. Dr. U. Kunz, Prof. Dr. T. Turek*

1 – 17

In Situ Determination of the Potential Distribution within a Copper Foam Electrode in a Zinc-Air/Silver Hybrid Flow Battery